

MICROSTRUCTURAL CHARACTERIZATION OF PRIMARY WATER STRESS-CORROSION CRACKS IN ALLOY 182 WELDS FROM PWR COMPONENTS AND LABORATORY TESTS

L.E. Thomas, M.J. Olszta, B.R. Johnson and S.M. Bruemmer

Pacific Northwest National Laboratory, PO Box 999, Richland, WA, 99354, larry.thomas@pnl.gov

Intergranular stress-corrosion cracking of Alloy 182 welds in PWR primary water service was investigated by analytical electron microscopy of cracks and leading grain boundaries. Samples from crack-growth tests in simulated PWR and BWR water were also examined for comparison with service samples from several PWRs. Observations of the crack-tip microstructures indicated that the cracks propagated by interfacial attack around closely spaced $Cr_{23}C_6$ and $(Nb,Ti)C$ particles, and along the short boundary spans between the carbide particles. Characteristic corrosion microstructures found along cracks in the service samples included oxidized and partially dissolved carbide particles, as well as 5- to 8-nm-wide oxide-filled corrosion 'tunnels' along dislocations near the crack surfaces. The sample tested in simulated PWR primary water reproduced the characteristic crack microstructures found in the service samples, including the nm-scale tunnels. Cracks in the specimen tested in oxidizing-water containing sulfate differed by forming preferentially to one side of the carbide-decorated grain boundaries, and did not show the tunnel attack along crack walls. Comparisons with previous observations in Ni-base Alloy 600 suggest that the same underlying mechanism of penetrative IG corrosion may be responsible for PWSCC in both materials.

I. INTRODUCTION

Ni-base alloy 182, which is commonly used as a weld material for joining dissimilar metals in pressurized- and boiling-water water reactors (PWRs and BWRs), has proven susceptible to intergranular stress-corrosion cracking (IGSCC) in service. Instances of weld failure in pressure-vessel head penetrations have received considerable attention and led to investigations of the underlying mechanistic causes.¹⁻⁴ Although the possibility exists that the in-service cracks might have initiated at preexisting defects such as hot cracks or ductility-dip cracks produced during the welding process, examinations of cracked components have neither shown any evidence of such defects. On the contrary,

examinations by analytical transmission electron microscopy (ATEM) have revealed the presence of corrosion products indicating penetration by high-temperature water throughout the crack, and pointed to primary-water SCC (PWSCC) as the cause of cracking.^{5,6}

Crack-growth tests have also demonstrated the susceptibility of Ni-base alloys including alloy 600, 182 and X-750 to IGSCC in simulated PWR water, with the highest cracking rates found at electrochemical potentials near the Ni/NiO equilibrium.^{7,8} These results have reinforced the idea that corrosion/oxidation processes at the crack tips control the cracking rate. Recent tests for alloy 182 evaluating aqueous H_2 effects on SCC growth rates in simulated PWR primary water at 325°C have demonstrated the same electrochemical dependence of cracking that has been well-documented in alloy 600 and other Ni-base alloys.^{9,10}

Previous ATEM studies of alloy 182 weld failures from several PWRs have determined that the cracking occurred along high-angle grain boundaries that formed between dendrite colonies during the weld solidification.^{5,6} The TEM studies further indicated that narrow penetrative attack along the grain boundaries led the cracking. This paper extends the earlier work to include observations from a head-penetration weld in the North Anna-2 PWR, and compares the in-service crack microstructures to ones produced during crack-growth tests under simulated PWR primary water and oxidizing BWR water conditions.

II. EXPERIMENTAL

II.A. Samples

The ATEM examinations of cracked welds from PWR primary-water service included samples from Ringhals-3 and -4, Davis-Besse, and North Anna 2. These samples as well as the ones from laboratory tests are identified in Table 1. The Alloy 182 samples covered in this paper came from 4 different PWRs and 2 laboratory crack-growth tests. The samples are identified in Table 1. Details of the Ringhals and Davis-Besse samples were given in earlier papers.^{5,6}

TABLE 1. Alloy 182 weld samples

PWR Service

Reactor	History
Ringhals-4	Circumferential cracks in TIG-repaired welds in outlet safe-end
Ringhals-3	Circumferential cracks in TIG-repaired welds in outlet safe-end
Davis-Besse	Axial cracks in J-welded head penetration
North Anna	Axial cracks in J-welded head penetration

Crack-Growth Tests

Test	Conditions
BWR water (GE C302)	Round-robin weld sample tested in normal BWR water (2 ppm O ₂) at 288°C. 30 ppb SO ₄ ²⁻ added.
PWR water (PNNL CT012)	Round-robin weld sample tested in PWR primary water with varied H ₂ at 325°C. Test ended with 5 cc/kg H ₂ (slightly off the Ni/NiO stability transition).

II.A.1. North Anna CRDM

The North Anna 2 sample came from a control rod drive mechanism (CRDM), Nozzle 31, with cracks in the alloy 182 J-weld joining an alloy 600 penetration pipe to the low-alloy pressure vessel steel. Figure 1 schematically illustrates the nozzle structure and crack location. Metallographic examinations of sections cut from the nozzle showed that multiple cracks had initiated from the primary-water surface of the weld and propagated axially to intersect both the alloy 600 and the pressure vessel steel. The cracks also reached the air gap between the pressure vessel steel and the alloy 600 pipe.

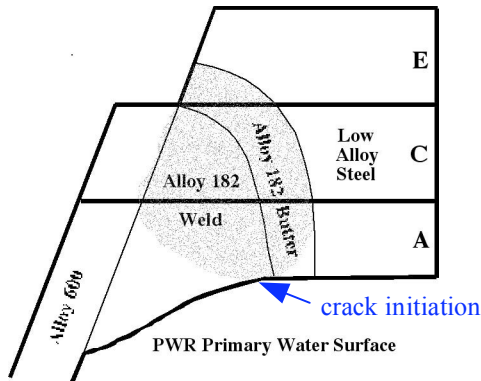


Figure 1. Axial crack location (shaded) in weld from North Anna-2 Nozzle 31. Letters refer to metallographic sections.

II.A.2. SCC Test in Hydrogenated PWR Water

CT012 was a crack-growth sample of alloy 182 weld metal that was tested at 325°C in simulated PWR primary water. The weld was used for round-robin crack-growth testing coordinated by the international Cooperative Group on Environment-assisted cracking. The heat

composition (wt%) was 12.3Cr, 8.2Fe, 7.0Mn, 0.44Si, 0.21Ti, 0.043C and 0.76(Nb+Ta) with the balance Ni.

This particular test involved multiple sequences at different hydrogen levels spanning the Ni/NiO stability regime. A detailed description of the test has been published previously.⁹ The final test sequence over the last 0.05 mm (50 μm) of crack length was run at 5 cc/kg H₂ in the NiO stability ECP region near the Ni/NiO stability transition. This condition coincided with the highest measured propagation rates. Data from this part of the test are reproduced in Figure 2. The TEM examinations focused on the deepest cracks in this cross-section, corresponding to the last region of SCC growth.

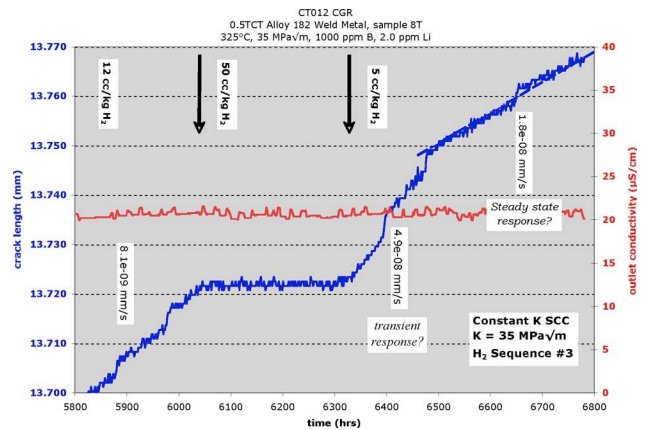


Figure 2. Crack-growth data for alloy 182 weld in simulated PWR primary water at 325°C. End-of-test sequence at 5 cc/kg H₂, near the Ni/NiO stability transition.

II.A.3. SCC Test in BWR Water Containing Sulfate

C302 was a crack-growth sample of Alloy 182 weld material that was tested in oxidizing BWR water (2 ppm O₂) at 288°C. It was tested in the as-welded condition.

During the last ~1000 hours of the test, 30 ppb SO₄²⁻ was introduced (as H₂SO₄) to promote rapid crack growth. The last ~0.7 mm of cracking was obtained under constant K conditions. Figure 3 shows the well-behaved crack growth at the end of the test, which corresponded to the sample region that was examined by TEM.

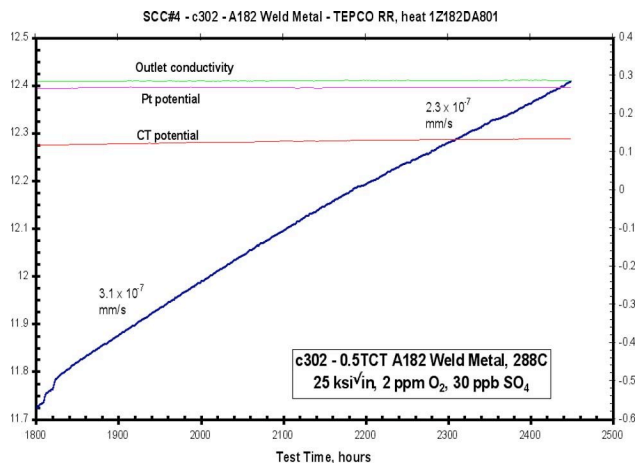


Figure 3. SCC response of Alloy 182 weld metal tested in 288°C water containing 2 ppm O₂ plus sulfate.

II.B. Methods

II.B.1. TEM Sample Preparation and Analysis

Cross-section samples containing crack tips were prepared for TEM examination by dimple grinding and ion micromilling. The samples were first vacuum-impregnated with low-viscosity resin and polished to reveal the cracks. Then thin wafers containing the cracks were cut out and glued to 3-mm-diameter Mo support washers with the targeted features at the centers. After trimming away excess material, the disk samples were flat-ground and finish polished to <100 μm total thickness from the non-washed side. The samples were dimple-ground from the washer side to ~15 μm thickness, and briefly ion milled with 5 keV argon ions at ±6° incidence to improve the surface finish for scanning electron microscopy (SEM) examinations. Following the SEM examination, ion milling was continued to develop thin areas suitable for TEM analysis. Final milling was performed at reduced energy and beam incidence (2 keV, ±4°) to minimize superficial ion-beam damage. Repeated cycles of thinning and observation were used to produce optimum local sample thicknesses for high-resolution ATEM examination.

SEM examinations were performed using backscattered electron (BSE) imaging to reveal the large-scale characteristics of cracks and second-phase particles by average-atomic-number contrast and the grain structures by crystallographic orientation contrast. Computer-controlled elemental mapping by energy-dispersive x-ray spectrometry (EDS) was also extensively applied in the SEM to observe the compositional variations of nearly all elements (down to boron). Beam spreading in the samples limited the SEM/EDS map resolutions about 1 μm.

ATEM examinations were performed with a 200 kV field-emission-gun (FEG) instrument that allowed

microstructural imaging and analysis at resolutions down to nm and sub-nm scales. Fine-probe EDS analysis and mapping in the scanning transmission (STEM) mode were extensively used to characterize the compositions of corrosion products and grain boundaries. Computer-controlled drift correction during line-profile and map acquisitions yielded spatial resolutions as low as ~1 nm. The detection limits for most elements were ~1 wt% in x-ray mapping and ~0.3 wt% for spot analyses. In special cases, spectral interferences affected the detection of a minor, lighter element in the presence of a major, heavier one. Important interferences in this work were O-K/Cr-L and S-K/Nb-L. TEM/EDS analyses were performed without correcting for x-ray absorption in the sample or for O-K/Cr-L interference. Results involving O should therefore be taken as strictly qualitative.

II.B.2. Atom Probe Tomography

Atom probe tomographic (APT) analysis was also used to examine the composition of a weld grain boundary in the round-robin sample. This preliminary effort complemented the ATEM/EDS analyses of major elements, and additionally provided a means for probing segregation of otherwise hard to detect elements such as B, C, N, and O at concentrations down to a few atomic ppm. Needle-shaped samples containing selected grain-boundary regions were prepared by Focused Ion Beam (FIB) micromachining, and analyzed in an IMAGO Localized Electrode Atom Probe (LEAP™) instrument. Suitable grain boundaries were noted as those with traces longer than 20-30 μm and as straight as possible. The LEAP analysis uses pulsed laser evaporation and position-sensitive time-of-flight ion detection to analyze ~50% of the atoms from the needle tip. Finding a sample with a suitably oriented grain boundary usually required several tries. Each sample analysis was performed until ~10-15 million atoms were collected by the detector, or the feature of interest (in this case, the grain boundary) was captured. Data analysis was then performed using the Imago IVAS analysis program. The method allows three-dimensional reconstruction of the data with near-atomic resolution. Minor S in the sample was not detectable due to strong interferences with the major element Ni.

III. OBSERVATIONS

III.A. North Anna-2 CRDM

Metallographic examinations of polished sections from the North-Anna-2 J-groove weld showed that multiple cracks had initiated at the primary-water surface in the weld butter region, and had propagated through the weld metal to intersect both the alloy 600 and the pressure vessel steel. Figure 4 gives a low-magnification view of the cracks and a detail view of one region that was

targeted for TEM sample preparation. The periodically segmented appearance of the crack in this section may reflect the weld structure or stresses, although this is not known for certain. Relatively wide crack openings suggested that the cracks had opened under high stresses. Despite the appearance of discontinuous cracks on cross sections, the presence of corrosion products throughout the cracks indicated an interconnected crack network that had been fully penetrated by high-temperature water.

The metallographic examinations also showed that the cracks coincided with grain boundaries in the weld metal. These boundaries had a characteristically wavy, serpentine appearance reflecting formation by dendrite impingement during solidification. Apart from minor occurrences of grain-boundary migration, the boundaries where cracking occurred were both crystallographic grain boundaries and interdendritic boundaries.

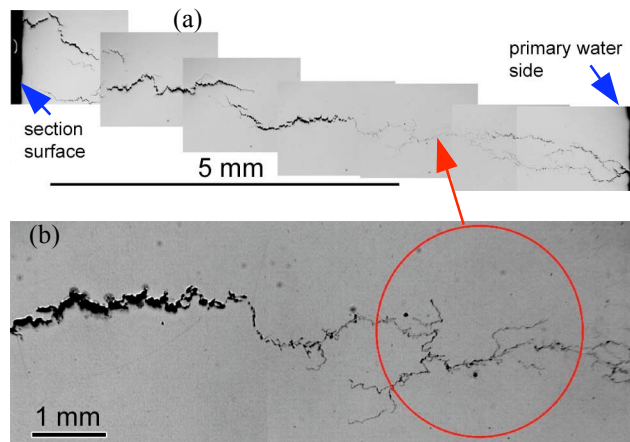


Figure 4. Optical micrographs of North Anna CRDM cross section showing main crack running through entire section thickness. Scale marker length 5 mm. Circle in lower figure represents size of 3-mm-diameter TEM disk.

Since the crack traversed the entire width of the section and thus did not contain a unique primary tip, TEM samples were prepared from the middle of the section. Extensive crack branching yielded many secondary tips that were suitable for ATEM. SEM/BSE images of a TEM sample, shown in Figure 5, further illustrate the appearance of the cracks and their relation to grain boundaries. The mottled crystallographic contrast of the grain images is characteristic of strained material. Zooming in on the higher magnification micrograph in Figure 5 reveals scattered 0.2- to 1- μ m-diameter second-phase particles throughout the grains and along the grain boundaries the white-appearing particles are predominantly Nb carbides and the dark particles were mainly TiC. As shown later, the grain boundaries were heavily decorated by fine NbTi carbide and Cr-carbide particles. These smaller particles were generally too small to observe at the relatively low magnifications of the SEM.

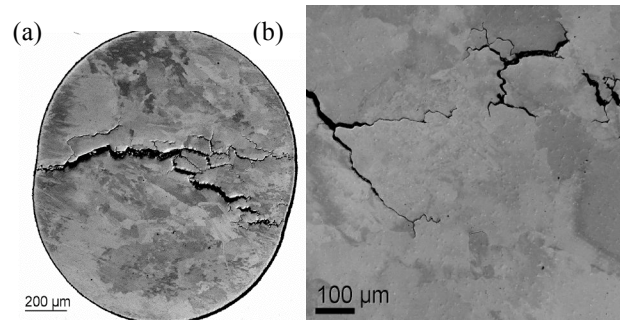


Figure 5. SEM/BSE images of TEM samples prepared from crack area North Anna 2 CRDM weld. Taken from dimple-polished side with support washer after brief ion milling.

EDS maps taken in the SEM reveal the weld compositional microstructures in relation to the grain boundaries and cracks. Low-magnification maps and the corresponding BSE image shown in Figure 6 provide an overview of the weld dendritic structures. A secondary crack tip appears at the left side of the image area, and the O-K map indicates that the crack was filled with oxide. The major feature of this map set, however, is the dendritic structure revealed as patterns of constitutional segregation. The Fe-K map, in particular, clearly shows the dendritic structures of the individual grains. These compositional structures each have a regular alloy framework of Fe- and Cr-rich regions with interstitial Mn and Si-rich regions of the last-solidified material. Qualitative compositional analyses from the SEM/EDS data indicated that the high-Mn regions were enriched by ~3-5 wt%, and the high-Si regions were enriched by ~2 wt%, compared to the Fe-Cr-rich regions. The elemental maps reveal Nb, Ti, Mn, Al-rich particles.

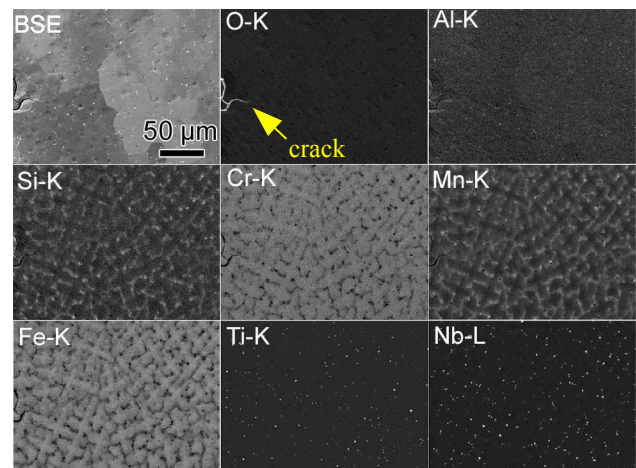


Figure 6. SEM/EDS elemental maps showing weld segregation and precipitation in North Anna 2 sample.

Figure 7 shows a color composite image made by combining several maps to further demonstrate important relationships between the $\mu\text{-m}$ -size second-phase particles, the dendrite structures, and the grain boundaries. This image is a composite of maps for Nb (black), Ti (green), high Mn (blue) and low Mn (yellow), and is superimposed on the BSE image. Blue spots in the high Mn map indicate MnS particles. (EDS point analyses were used to identify the S in the MnS particles because spectral overlap between S-K and Nb-L x-rays prevented directly mapping the S). The Nb (carbide) and MnS particles can be seen to coincide with the Mn-Si alloy regions of the dendrites. The Ti-rich particles (probably TiC or Ti(C, N)) show a weaker correlation with the dendrite segregation, usually appearing in the Mn-Si-rich regions, but sometimes also in the Fe-Cr-rich areas.

Comparing the Mn-Si-rich regions with the BSE image shows a moderate correlation of these areas with the grain boundaries. About 50% of regions along the grain boundaries coincided with high Mn and Si locations, but many others coincided with the high Fe and Cr locations. Other areas containing cracks showed a similarly weak correlation between grain boundaries and the constitutional segregation and $\mu\text{-m}$ -scale precipitation from the dendrites. The $\mu\text{-m}$ -size carbides and MnS particles produced during weld solidification appeared at approximately the same frequency along the grain boundaries as they did in the grain interiors. Further comparisons made by overlaying various elemental maps indicated no O in the intragranular particles and no correlation of the Al-rich particles with the other particles.

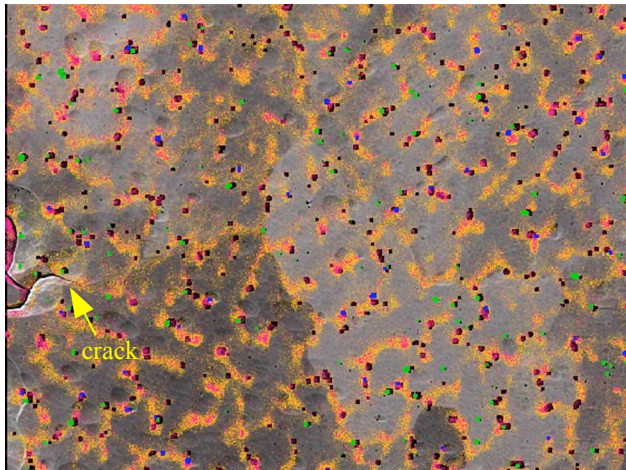


Figure 7. Color composite of SEM/EDS maps illustrating correlations between weld dendritic microstructure, second-phase particles and grain boundaries. color key: yellow -Mn; pink -Si, black -NbC particles; green -TiC particles; blue -MnS particles

TEM examinations of the North Anna weld samples focused mainly on the crack tips and leading grain boundaries. As illustrated by Figures 8 and 9, the

cracking occurred along grain boundaries that were decorated by closely spaced 30- to 50 nm-diameter Cr-carbide particles and 5- to 10-nm-diameter NbTi carbides.

Electron diffraction analyses identified the Cr carbides as cubic Cr_{23}C_6 and the NbTi carbides as cubic MC. The STEM/EDS maps in Figure 9 distinguish the particles by their compositions, and illustrate how the particles become interfacially attacked, convert to oxide, and begin to dissolve in the crack. For descriptive purposes, the leading edge of the oxidation along the attacked grain boundaries and particle interfaces is referred to as the crack tip.

Interfacial attack around the Cr carbide particles near the crack tip can be seen by comparing the particle images in the O-K and Cr-K maps. Due to partial spectral superposition of Cr-L and O-K x-rays, the oxidized and unoxidized regions of the particles both appear highlighted on the O-K map. The oxidized shells around the attacked particles appear brighter than the unoxidized cores. In the Cr-K map, the oxidized shells appear fainter than the cores.

Another effect shown by the EDS maps is the apparent dissolution of the carbide particles in the crack, starting at short distances behind the crack tip. This is indicated by a decrease in particle intensities on the Cr, Nb and Ti maps.

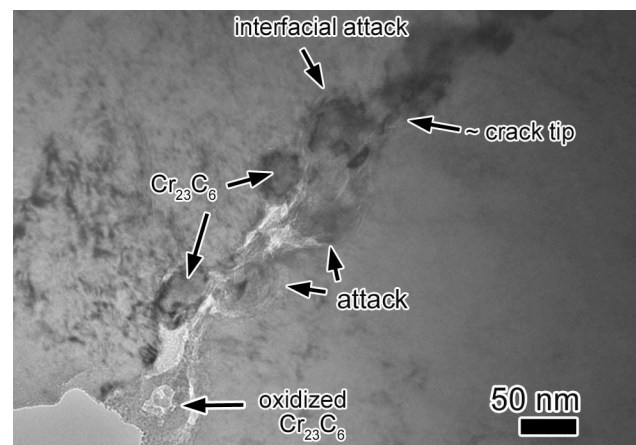


Figure 8. Crack tip region in North Anna 2 TEM sample. Shows degraded carbide particles behind crack tip and interfacial attack along the particle interfaces at the tip.

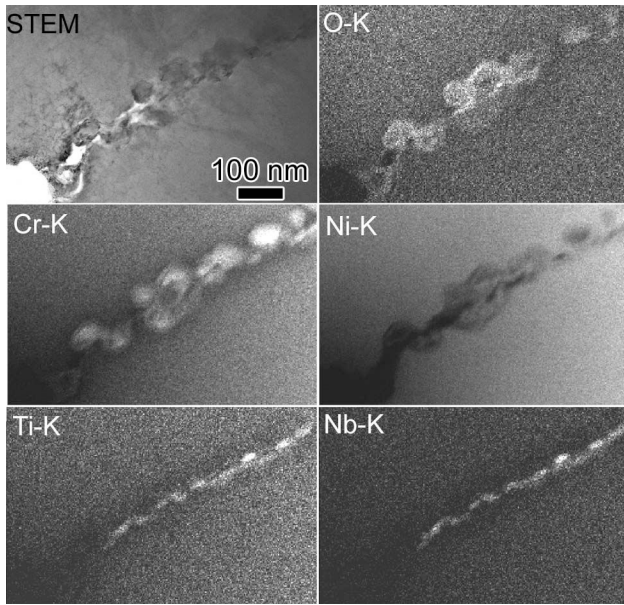


Figure 9. STEM EDS maps of crack tip area in previous figure. Shows interfacial attack (oxidation along particle interfaces at the tip) and apparent dissolution of degraded carbides in crack.

In another tip example, shown in Figure 10, the crack ended along a locally straight section of grain boundary near a cluster of μm -size NbC particles. The tangled dislocation structure of the weld metal can be seen in a strongly diffracting region just ahead of the crack tip. Higher magnification brightfield and oxide darkfield images of the tip region in Figure 10(b) and (c) highlight the interfacial attack around fine IG carbide particles, and polycrystalline MO-type oxide in the crack. The exact location of the tip is hard to pinpoint, but is best judged from the oxide darkfield image. The oxide narrowed to less than 10 nm wide at the tip.

Crack regions near the tips were filled with corrosion products oxide and remnants of the attacked IG carbides. Figure 11 shows an example of the attacked and degraded structures ~ 0.5 to 1 μm behind the crack tip. Degraded microstructures in this area included the oxide corrosion products and remnants of the attacked IG carbide particles in the crack, and filamentary corrosion tunnels in the adjacent metal. ATEM analyses indicated a complex set of corrosion products in these structures. Although further analyses would be needed to identify all the oxide phases in this area, diffraction analyses identified polycrystalline cubic MO-structure oxide as the main corrosion product in the cracks. The oxidized shells around altered Cr-carbide particles were tentatively identified as Cr_2O_3 .

The oxide-filled corrosion tunnels observed in the metal near the crack tips appeared similar to those reported earlier from alloy 182 welds in the Ringhals and Davis-Besse PWR samples. These tunnels were 5 to 8

nm in diameter and extended to ~ 100 -150 nm below the surfaces of the cracks. The oxide in them had a spinel structure with the same orientation as the metal matrix. Darkfield images taken with spinel reflections showed the oxide in the tunnels as discrete 5-8-nm diameter crystallites. The tunnels evidently formed along dislocations in the metal.

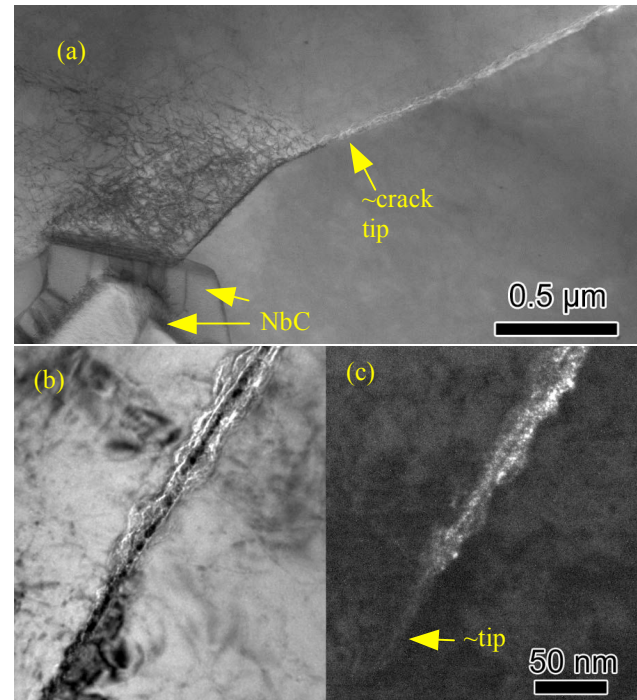


Figure 10. Second crack tip in North Anna weld sample. (a) STEM overview with grain boundary on edge. (b) TEM brightfield and (c) MO oxide darkfield images.

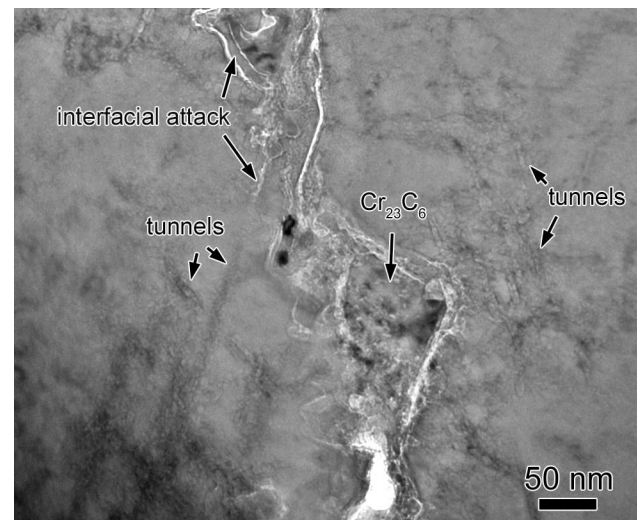


Figure 11. Degraded microstructures near crack tip in North Anna weld. Shows interfacially attacked carbides in crack, and oxide-filled 'tunnels' formed along dislocations in the adjacent metal.

Figure 12 shows the results of fine-probe EDS line scans taken across the corrosion tunnels. The composition profiles indicated Cr and Mn enrichment of the spinel crystallites in the tunnels. Scans taken along tunnels (results not shown) indicated that the tunnel structures consisted of the Cr-Mn-rich spinel crystallites separated by Ni-rich metal. As also indicated by the results, the tunnels also contained spots of concentrated S (up to ~ 2 wt.% through the local foil thickness). High S concentrations were also observed previously in similar corrosion tunnels from the Davis-Besse alloy 182 weld sample. Scans taken across unattacked dislocations ahead of the tunnels showed no detectable segregation of any alloying elements such as Nb or Ti, nor any S segregation at the dislocation cores.

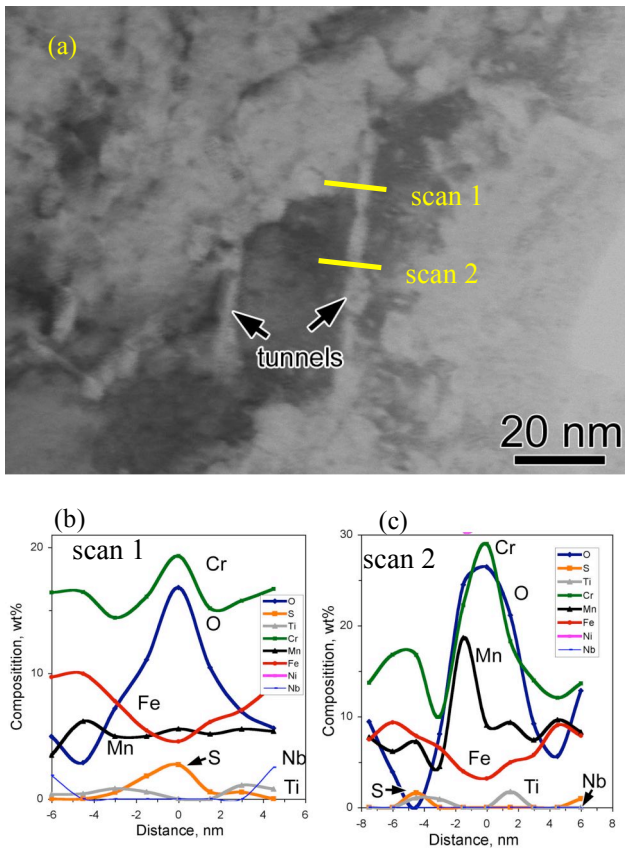


Figure 12. EDS composition profiles across corrosion 'tunnels' near crack tip in North Anna 2 alloy 182 weld sample.

III.B. PWR Water Test Sample

This alloy 182 crack-growth test in simulated PWR primary water produced disconnected-appearing SCC cracks along approximately parallel grain boundaries. As shown by an overview image of the cross-sectioned test sample in Figure 13(a), the cracks occurred parallel to the elongated grain structure of the weld. A higher

magnification view of the tip region in Figure 13(b) shows that initial IGSCC during final crack transitioning and at constant K was highly non-uniform. The cracks had the serpentine appearance of grain boundaries produced by dendrite impingement during weld solidification. Despite the discontinuous-connected appearance of the cracks in cross section, the presence of oxide corrosion products throughout them indicated that the cracks had been completely penetrated by high-temperature water. The post-test SCC fracture surface shown in Figure 13(c) also suggests that the grain boundary where cracking occurred also corresponded to a dendrite boundary.

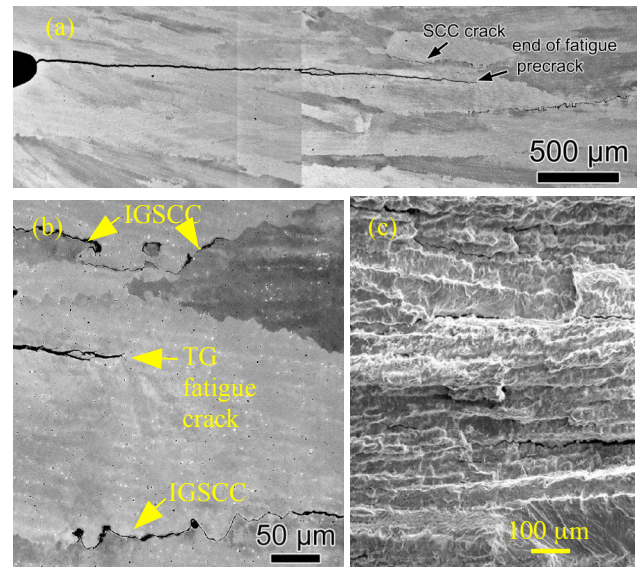


Figure 13. Cracks in Alloy 182 weld from test in simulated PWR primary water. (a) Low-magnification SEM/BSE overview of metallographic section. (b) TG to IG crack transition region. (c) IG fracture surface illustrating interdendritic fracture morphology.

Microstructural characterization of the alloy 182 weld sample by TEM confirmed the grain-boundary decoration by 10- to 20-nm diameter $Cr_{23}C_6$ particles and smaller MC ($M = Ti + Nb$) particles. Both kinds of particles appeared irregularly distributed along the boundaries. Fine-probe EDS analysis and mapping in the TEM indicated the Nb, Ti and minor Si, but no other significantly segregated impurities down to the detection limits of these methods. Grain boundary composition profiles between $M_{23}C_6$ carbides indicated strong Cr depletion with levels down to ~5 wt% (matrix 13–15 wt%), however neither the $M_{23}C_6$ particles nor the Cr depletion were continuous along the boundaries examined. Finally, a high dislocation density was present throughout the weld metal microstructure.

Additional grain boundary characterization has been performed by APT analysis to further probe for evidence of segregation, including light elements such as B and C. This was a pioneering effort that has only yielded preliminary results. As shown by results given in Figure 14, the APT method revealed minor segregation of Si, B, P and C on the grain boundaries. The data reconstruction given at the top of the figure illustrates the Si segregation along a grain boundary between carbide particles. As further shown by reconstructed line profiles at the lower part of this figure, the Si reached ~1.5 at% at the boundary, vs. ~0.8% in the matrix. Boron, C and P were also enriched at the grain boundary, although their maximum concentrations were less than 0.15 at%. No other significant impurity segregation was found. Of the major elements, the results indicated strong local Cr depletion at the boundary, at least in this limited analysis.

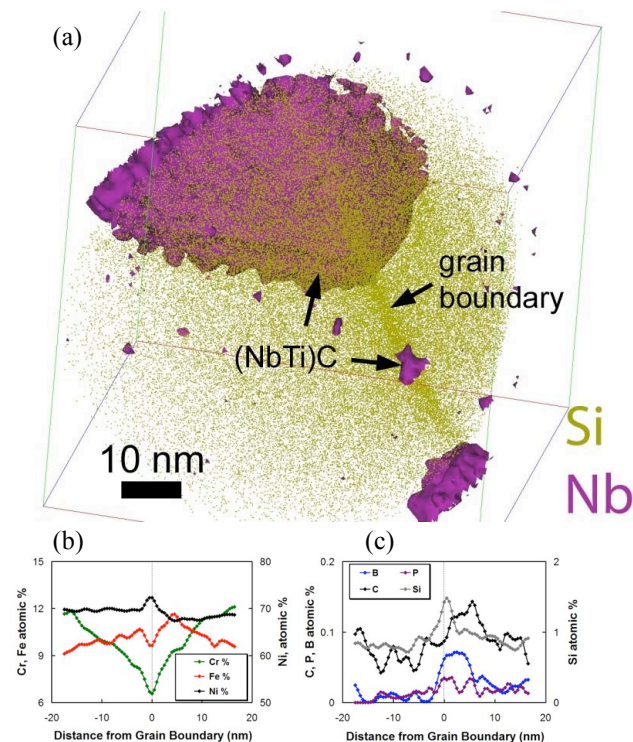


Figure 14. APT analysis of grain boundary in Alloy 182 weld. (a) Data reconstruction for Si and Nb, showing grain boundary on edge and Si segregated along boundary. (b,c) Reconstructed line profiles for major and minor elements.

TEM observations of the PWR test sample described here again focus primarily on the crack tip regions. Where the cracked narrowed near their tips, they appeared filled with polycrystalline corrosion product oxides. Diffraction analyses of these regions indicated that both spinel and NiO-type oxides were present, as well as remnants of the original and altered (Nb,Ti)C and Cr_{23}C_6 carbides from the original bulk grain boundaries. Figure

15 shows an example of these structures with selective darkfield imaging used to identify the phases. STEM/EDS maps of the same crack area, in Figure 16, show the extent of the oxide and indicate the partial dissolution of Cr carbide and MC particles in the crack. Remnants of the intergranular MC carbides appear as small Nb and Ti-rich spots at the crack walls.

Other TEM images taken under under- or overfocus conditions revealed corrosion tunnels in the metal, similar to those observed along crack walls in all the PWR service samples. The tunnels are shown by an overfocus image in Figure 17. Diffraction patterns from the areas with tunnels showed the presence of oriented spinel oxide in the metal, and darkfield images taken with spinel reflections also showed that the 5- to 8 nm-wide 'tunnels' were filled with this oxide. The observation of these corrosion tunnels in the weld sample that was tested in PWR primary water indicated that the test reproduced one of the most distinctive features of the cracks from service samples. As was also found in the service samples, the tunnels formed in the cracks behind the attack fronts.

High-resolution STEM/EDS maps in Figure 18 show one of the crack tip regions. The tip location where the oxide ended can be identified from the O-K map. The Cr-K map shows Cr_{23}C_6 particles along the grain boundary ahead of the crack tip, and partially attacked particles immediately after the tip. The MC particles in this region did not show any indication of corrosion attack. Also, no significantly elevated Ni concentrations appeared in the metal ahead of the cracks, in contrast to observations in other Ni-base alloys (such as alloy 600) with cracks produced in PWR water environments. In the grain boundary region ahead of the crack tip in Figure 18, the Cr map highlights the Cr_{23}C_6 particles and indicates a strong depletion of Cr near the particles.

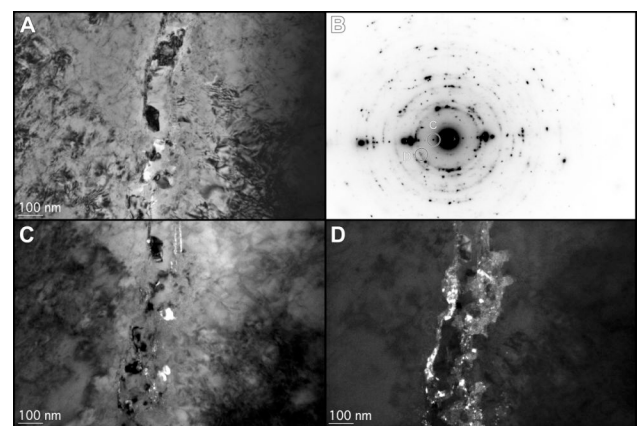


Figure 15. Analysis of oxide-filled crack region near tip in alloy 182 PWR crack growth specimen. (a) TEM brightfield (a), (b) selected area diffraction pattern, (c) darkfield image taken with a reflection from Cr_{23}C_6 , and (d) darkfield image highlighting polycrystalline MO-structure oxide.

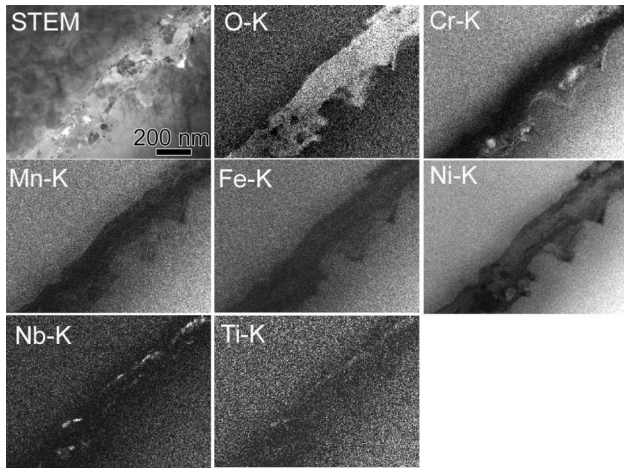


Figure 16. STEM EDS maps of oxide-filled crack region near crack tip in PWR-water test sample

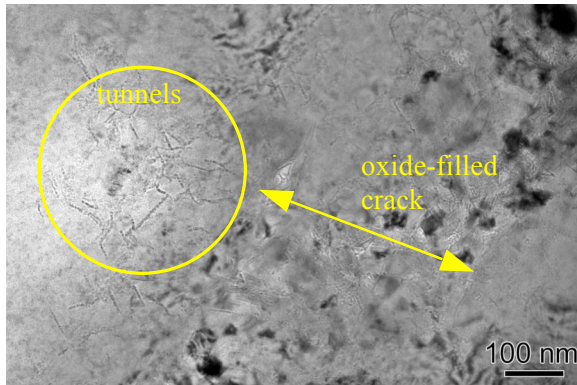


Figure 17. Corrosion tunnels in the metal along an oxide-filled crack in PWR-water test sample. Tunnels appear dark in overfocus image.

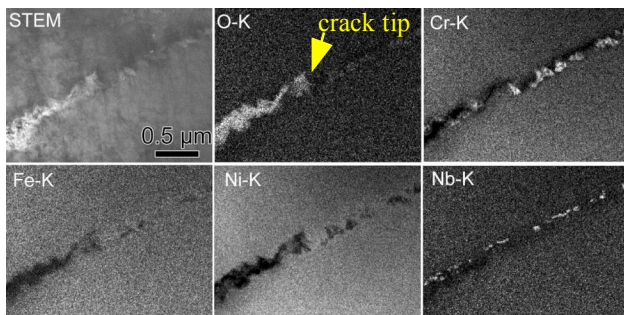


Figure 18. EDS maps of crack-tip region in CT012. Crack appears somewhat inclined in these images.

III.C. BWR Water Test Sample

The alloy weld microstructures observed in this crack-growth test sample appeared similar to those already described. General features included an elongated grain structure with minor intragranular compositional fluctuations and crenulated grain boundaries reflecting the dendrite structures and weld solidification patterns. As

was also observed in the other weld samples, 0.5- to 1- μm particles of mainly Nb- and Ti carbide appeared throughout the grain interiors and sporadically along the grain boundaries. TEM examinations also showed that the grain boundaries were decorated with closely spaced 20-nm-diameter particles of Cr_{23}C_6 and finer MC particles containing both Nb and Ti. High densities of tangled dislocations were observed throughout the weld metal.

Multiple SCC cracks occurred along the weld grain boundaries ahead of the transgranular precrack in the test sample. Often, these cracks appeared significantly deviated from the direction of the fatigue precrack. Figure 19 illustrates the weld grain structure and typically wavy appearance of the IGSCC cracks that formed near the end of the test. The mottled crystallographic contrast in this image is characteristic of highly strained metal.

TEM observations of narrow cracks in the BWR-water test sample generally showed uniform, 30- to 50-nm-thick films of oriented cubic MO-type oxide along the walls and polycrystalline corrosion product with a sheet-like structure filling the crack centers. Figure 20 shows the wall oxide films and crack-fill material. Diffraction ring patterns from the crack-fill product did not match any standard patterns in the EDD database (the closest match was to the cubic MO structure). Most likely, this product was an unidentified hydroxide.

EDS analyses indicated that the fill product consisted of relatively Cr-rich (compared to the metal matrix) Ni-Cr-Fe oxide. The single-crystal oxide films next to the metal contained Fe, Cr and Ni with slight Ni enrichment relative to the metal matrix. Additionally, the analyses indicated up to ~6 wt% S in the fill product, and local regions with high Si. The presence of high S in the crack corrosion products in this sample is notable and consistent with the addition of 30 ppb SO_4 to the oxidizing BWR water environment.

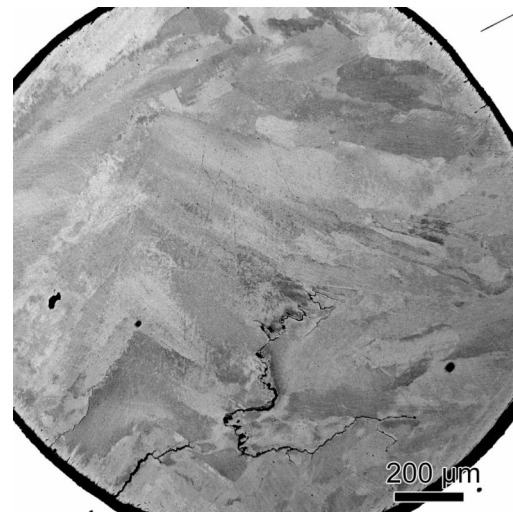


Figure 19. Alloy 182 TEM sample from SCC test in oxidizing BWR water plus sulfate.

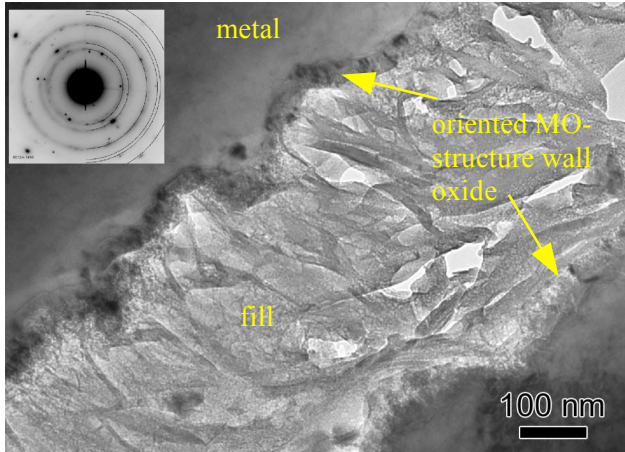


Figure 20. Loosely-filled crack in Alloy 182 TEM sample from CG test in BWR water. Inset diffraction ring pattern from fill product approximately matched cubic MO.

As the cracks narrowed, the oriented wall oxide films became the predominant corrosion product. A narrow band of fine-grained oxide containing high S continued to the crack tips. The crack region shown in Figure 21 contained uniform 30 to 50-nm wide MO-structure films at the walls, and a central layer of nanocracked material. This figure shows a composite MO-darkfield image that was produced by combining oxide darkfield images from both sides of the crack (the images were taken using different MO spots from the diffraction patterns taken at the metal/oxide interfaces of both matrix grains.) Composition profiles across the crack in this area are shown in Figure 21(b). The profiles indicate an asymmetrical crack microstructure with a Cr-rich region at one side corresponding to the location of Cr-carbide particles along the original grain boundary. This, and other profiles obtained from cracks in this sample, suggested that the cracking occurred along one side of the originally carbide-decorated grain boundaries. The profiles in Figure 21 also indicate high S in the material along the crack center, as well as Si and Nb in the central layer. Additionally, the Cr-rich regions along one side of the crack coincided with high O, indicating that the carbides had been at least partially oxidized.

STEM/EDS maps of the same area, given in Figure 22, show the partially oxidized remnants of Cr carbides and smaller MC-type carbides in the narrow crack. The maps also showed losses of Mn, Fe and Ni in the crack.

TEM observations of several crack tips in the BWR water test specimen showed the epitaxial MO oxide films along the crack walls tapering very gradually before ending along the carbide-decorated grain boundaries. The epitaxial oxide formation was preceded by one-sided attack along the carbide particle interfaces. This highly localized attack produced 'cracks' only a few nm wide on one side of the carbide particles. Figure 23 shows a tip

example with the image contrast enhanced to improve the crack visibility. It is difficult to tell exactly where the narrow attack ended.

Another crack-tip example in Figure 24 includes results of a fine-probe EDS line scan analysis across the oxidized zone at the tip. The oxide narrowed to a few nm just ahead of where the line scan was made. Composition profiles in this figure show the oxide region displaced to one side of a Cr carbide particle. This analysis also detected Nb and Ti (not plotted) apparently from an MC particle. However, no S was detected this close to the crack tips.

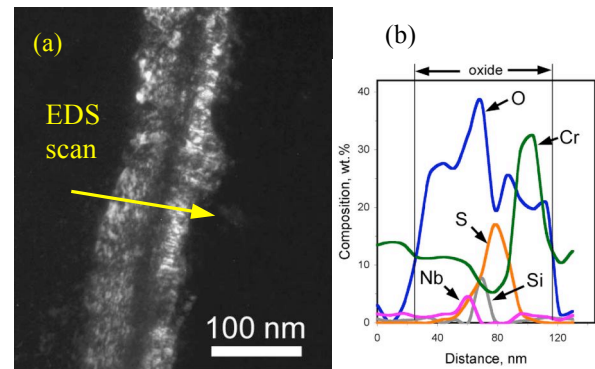


Figure 21. Narrow IG crack in Alloy 182 sample from BWR-water test. (a) Superimposed oxide darkfield images of oriented MO-type oxide films on both sides of crack. (b) Composition profiles from line scan.

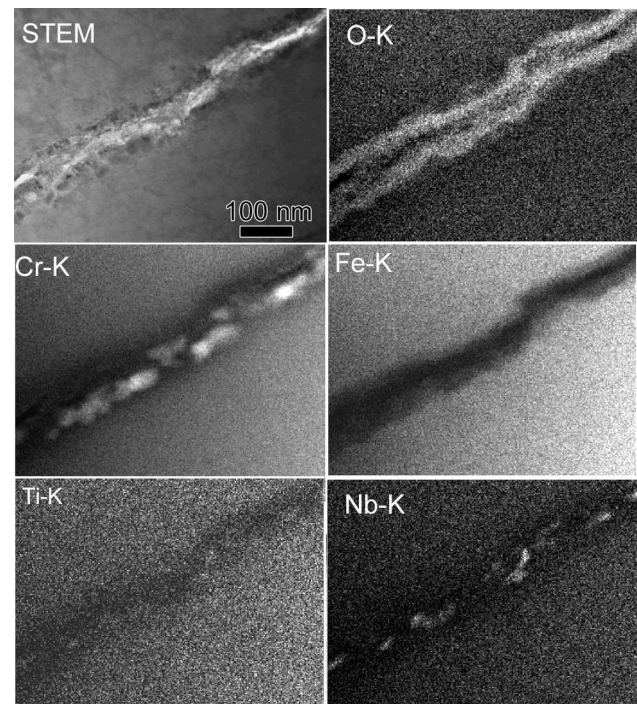


Figure 22. STEM/EDS maps of near-tip crack in BWR test specimen.

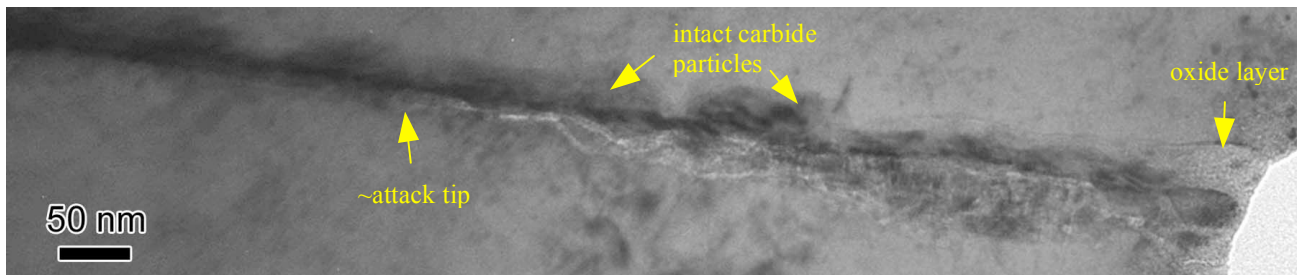


Figure 23. Crack tip in BWR-water test sample. TEM brightfield image enhanced to show asymmetrical attack at tip.

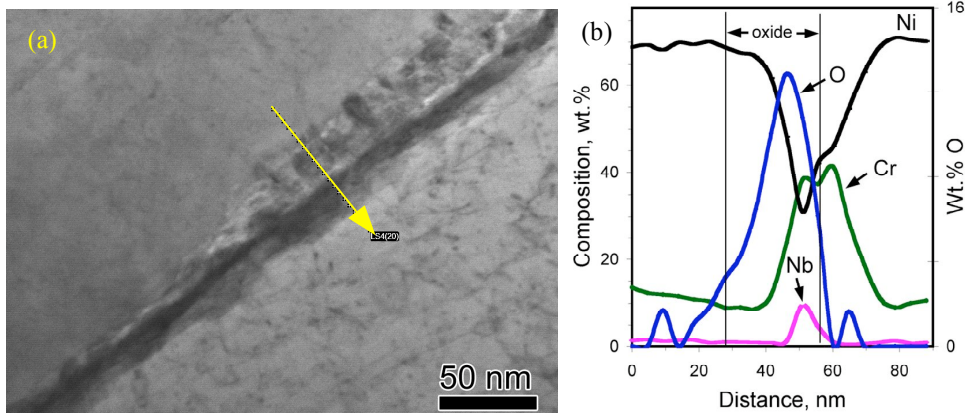


Figure 24. Line scan EDS analysis near crack tip in BWR-water test specimen. (a) STEM image. Arrow indicates scan location. Composition profile in (b) shows asymmetrical oxide formation at IG carbide particle.

IV. DISCUSSION

High-resolution ATEM characterizations of cracks and crack tips in well-controlled crack-growth test samples and LWR service samples enable a direct assessment of cracking processes at the nanoscale. The focus of the current work is the comparison of IGSCC occurring in Ni-base alloy 182 welds in PWR primary water service and in laboratory test environments including both hydrogenated (low ECP) PWR primary water and oxidizing (high ECP) BWR water. This comparison showed that the laboratory test with simulated PWR primary water did a good job of reproducing the characteristic crack microstructures observed in the PWR service samples. These characteristics included cracking led by narrow interfacial attack along the weld grain boundaries and IG carbide particles, rapid oxidation and subsequent dissolution of carbide particles soon after they became exposed to the crack environment, and the formation of distinctive few-nm-wide, 100 to 200-nm-long corrosion 'tunnels' along dislocations that intersected the crack walls.

In contrast, the crack microstructures observed in a specimen tested with oxygenated BWR water plus sulfate test differed significantly from those of the cracks produced in PWR primary water. Although the crack tips in the BWR-water test specimen also showed nm-scale

oxidation along the carbide-decorated grain boundaries in the welds, the attack followed one side of the particles, leaving the other side of the particles unattacked. Since the IG Cr_{23}C_6 particles formed with a parallel orientation relationship to the metal grains on either side of the grain boundary, and therefore have one coherent interface and one incoherent one, it has been suggested that this attack might have occurred preferentially along the incoherent interfaces. This possibility in the BWR water test sample was not investigated in the present work. In the case of cracks produced in PWR primary water, the leading IG attack appeared to fully envelop the carbides with no evident preference for the coherent or incoherent sides.

Other differences between the BWR and PWR water samples included the oxide crystallinity (oriented single-crystal oxide films in the BWR case versus polycrystalline oxide in the PWR specimens), and the consistent appearance of the corrosion tunnels at the metal crack walls near tips in the PWR specimens. These observations suggest a difference in effect of the two different water environments on the corrosion behavior in the cracks. The formation of oriented cubic oxide of either MO or spinel type may be an indication of the direct oxidant of the metal along the crack walls. From a crystal structure viewpoint, such oxide formation where the oxide and metal crystal structures are commensurate can occur without rearranging the atomic framework of the metal. Formation of a polycrystalline corrosion

product requires a complete atomic rearrangement, and is more likely the result of a dissolution and reprecipitation process. The oriented spinel crystallites found to fill the corrosion tunnels in PWR primary water would also be expected to form by directly oxidizing the metal along the dislocation cores.

Because the grain boundaries where SCC cracking is observed in the weld metal are by their origin both crystallographic grain boundaries and interdendritic boundaries produced during the weld solidification, the possibility exists that interdendritic segregation and precipitation could effect the weld cracking. The microstructural examinations and compositional analyses performed during this work, as well as in the earlier investigation of alloy 182 cracks from PWR service, indicated surprisingly little interdendritic segregation or precipitation in the welds. As shown by elemental maps produced in the SEM, compositional fluctuations within the weld dendrites create modulated structures with nodal points periodically enriched in Mn, Si, Nb, Ti and S throughout the grain interiors. (The S appears as MnS particles and the Nb and Ti form carbides at these points). Although the enriched (or precipitated) nodal points also appear along the grain boundaries in some places, such occurrences appeared nearly random. Similarly, TEM analyses at much higher spatial resolution have not shown significant impurity segregation at the boundaries.

Efforts to probe the weld grain boundaries with much greater sensitivity and detectability for minor element segregation have also been initiated using APT. The first analysis, performed on the round-robin alloy 182 weld sample that was used in the PWR water test, showed only minor enrichment of Si, B, C and P. Of these elements, only Si has been shown to promote IGSCC in Ni-base alloys.¹¹ These results, although very limited and preliminary at this stage, support the conclusion that limited segregation has occurred at the alloy 182 weld grain boundaries.

Although the TEM observations of grain boundaries in the welds have also shown that the boundaries are heavily decorated by fine Cr-carbide and MC carbide particles, the occurrence of these particles suggests that they formed rapidly during the weld cooling or during reheating in the successive weld passes. The lack of any other significant IG segregation observed either by ATEM or APT supports the speculation that the fine IG carbides did not form during the weld solidification.

The crack microstructures in alloy 182 welds from PWR primary water may also be compared to those of PWSCC cracks observed in mill-annealed alloy 600.^{12,13} Despite considerable microstructural differences between the convoluted, carbide-decorated boundaries in the weld alloy and the essentially straight, nearly carbide-free boundaries in MA alloy 600, and the compositional differences relating to Mn, Nb, Ti, and Si in the alloy 182, the two cases have in common IGSCC crack advance led

by extremely narrow penetrative attack along the grain boundaries. In both cases, the predominant corrosion product at the crack tips is a very fine-grained polycrystalline oxide with metal atom compositions not greatly different from those of the metal matrix.

V. CONCLUSIONS

1. Intergranular SCC of Alloy 182 welds in high-temperature water was studied by high-resolution microstructural and microchemical analyses of grain boundaries and cracks in samples from PWR primary water service and from laboratory tests with simulated reactor water.
2. SEM, TEM and APT revealed no strong solidification-induced impurity segregation or precipitation along the SCC-susceptible grain boundaries in the welds. These boundaries typically showed fine-scale precipitation of (NbTi)C and Cr₂₃C₆ carbides, plus minor segregation of Si and B along grain-boundary spans between the closely spaced particles.
3. A crack-growth test on alloy 182 weld metal in simulated PWR primary water reproduced the main crack corrosion microstructures found in service samples from several different PWRs, including interfacial attack around closely spaced IG carbides at the crack fronts and nm-scale corrosion tunnels in the metal along crack walls near the crack tips.
4. The crack and crack-tip microstructures of an alloy 182 weld metal specimen tested in oxidizing BWR water differed significantly from those produced in PWR primary water environments.
5. Despite considerable differences in the grain boundary microstructure and chemistry of Alloy 182 welds compared to MA Alloy 600, the narrow penetrative IG attack that appears to lead cracking of both materials in PWR primary water suggests a similar cracking mechanism.

ACKNOWLEDGMENTS

Support from various organizations were obtained for different aspects of this research including Rolls Royce and Associates and EPRI under contract DE-AC06-76RLO 1831, as well as the U.S. Nuclear Regulatory Commission and U.S. Department of Energy, Office of Nuclear Energy Sciences and Technology under Contract DE-AC06-76RLO 1830. Helpful interactions are recognized with Mychailo Toloczko, Bruce Arey and Peter Andresen along with Dieter Isheim and the Northwestern University Center for Atom Probe Tomography. Technical assistance of Ruby Ermi, Robert Seffens and Bruce Arey are also acknowledged. Pacific Northwest National Laboratory is operated for the U.S. Department of Energy by Battelle Memorial Institute.

REFERENCES

1. R.S Pathania, A.R. McIlree and J. Hickling, "Overview of Primary Water Cracking of Alloys 182/82 in PWRs," *Proc. Fontevraud V International Symposium: Contribution of Materials Investigation to the Resolution of Problems Encountered in Pressurized Water Reactors*, Fontevraud, France, 2002.
2. C. Amzallag, J. M. Boursier, C. Pages and C. Gimond, *Proc. 10th Int. Conf. Environmental Degradation of Materials in Nuclear Power Systems – Water Reactors*, Lake Tahoe, NV, NACE International, 2002, paper 32.
3. A. Jossen, K. Norrgard, J. Lagerstrom, G. Embring and D. Tice, "Cracking in Dissimilar Metal Welds," *Proc. of the 11th International Conference of Environmental Degradation of Materials in Nuclear Power Systems - Water Reactors*, Stevenson, WA, ANS, Illinois, 2003.
4. H. Xu, S. Fyfitich, J.W. Hyres, T.A. Lang and T.T Pleune, "Laboratory Investigation of PWSCC of CRDM Nozzle 3 and its J-Groove Weld on the Davis-Besse Reactor Vessel Head," *Proc. 12th Int. Conf. Environmental Degradation of Materials in Nuclear Power Systems*, Salt Lake City, UT, The Minerals, Metals and Materials Society, 2005, p. 833.
5. L. E. Thomas, J. S. Vetrano, S. M. Bruemmer, P. Efsing, B. Forssgren, G. Embring and K. Gott, "High-Resolution Analytical Electron Microscopy Characterization of Environmentally Assisted Cracks in Alloy 182 Weldments," *Ibid 3*, p. 1212.
6. L. E. Thomas, B. R. Johnson, J. S. Vetrano and S. M. Bruemmer, "Microstructural and Microchemical Characterization of Primary-Side Cracks in an Alloy 600 Nozzle Head Penetration and its Alloy 182 J-Weld from the Davis-Besse Reactor Vessel," *Ibid 4*, p. 567.
7. S. A. Attansao and D. S. Morton, *Ibid 3*, p. 143.
8. D. S. Morton, S. A. Attansao, G. A. Young and M. A. Ando, *Ibid 2*, p. 143.
9. S. M. Bruemmer, J. S. Vetrano and M. B. Toloczko, "Microstructure and SCC Crack Growth of Nickel-Base Alloy 182 Weld Metal in Simulated PWR Primary Water," *Proc. 13th Int. Conf. Environmental Degradation of Materials in Nuclear Power Systems-Water Reactors*, Whistler, BC, Canadian Nuclear Society, 2007.
10. P.L. Andresen, these proceedings.
11. P.L. Andresen and M.M. Morro, "Effect of Si on SCC of Irradiated and Unirradiated Stainless Steels and Ni-Base Alloys," *Ibid 4*, P. 87.
12. L. E. Thomas and S. M. Bruemmer, *Corrosion. J.*, 2000, 56, 572.
13. S. M. Bruemmer and L. E. Thomas, "Crack-Tip Examinations of Primary-Water Stress Corrosion Cracking in Alloy 600," *Proc. Fontevraud 6 International Symposium on Contributions of Materials Investigations to Improve the Safety and Performance of Light-Water Reactors*, French Nuclear Energy Society, 2006, p. 347.